

Article

Anticorrosion Property of Alcohol Amine Modified Phosphoric and Tannic Acid Based Rust Converter and Its Waterborne Polymer-Based Paint for Carbon Steel

Yang Chen ¹, Shiyu Li ¹, Zhiyong Liu ^{1,*} and Zixiao Wang ^{2,*} 

¹ School of Civil Engineering, Yantai University, Yantai 264005, China; 201800359014@s.ytu.edu.cn (Y.C.); hzlsy1995@163.com (S.L.)

² School of Civil Engineering, Wuhan University, Wuhan 430072, China

* Correspondence: lzy1698@163.com (Z.L.); zixiao.wang@whu.edu.cn (Z.W.)

Abstract: Four kinds of alcohol amines were tested to improve the anticorrosion performance of the phosphoric and tannic acid (PTA)-based rust converter. The alcohol amine modified PTA rust converters with the optimum mechanical and functional performances were used to prepare the homogeneous single-component waterborne rust conversion-based paint. The mechanical properties and the long-term corrosion resistance of the synthesized rust converter-based paint were investigated. The results show that alcohol amine modified PTA rust converter can convert the rust layer into a thick passivation film with iron tannate and iron phosphate as the main components, significantly improving the corrosion resistance of the carbon steel. The alcohol amine D modified PTA rust converter (RC-D) showed the best anticorrosion and rust conversion performances. The waterborne rust conversion-based paint can convert the rust layer of steel into a blue-black and relatively flat passivation film layer. The waterborne polymer-based paint containing 10 wt.% RC-D significantly improves the long-term corrosion resistance of the rusty steel and the mechanical property of paint.

Keywords: rusty carbon steel; rust converter; polymer-based paint; long-term anticorrosion



Citation: Chen, Y.; Li, S.; Liu, Z.; Wang, Z. Anticorrosion Property of Alcohol Amine Modified Phosphoric and Tannic Acid Based Rust Converter and Its Waterborne Polymer-Based Paint for Carbon Steel. *Coatings* **2021**, *11*, 1091. <https://doi.org/10.3390/coatings11091091>

Academic Editor: Alina Vladescu

Received: 10 August 2021

Accepted: 5 September 2021

Published: 9 September 2021

Publisher's Note: MDPI stays neutral with regard to jurisdictional claims in published maps and institutional affiliations.



Copyright: © 2021 by the authors. Licensee MDPI, Basel, Switzerland. This article is an open access article distributed under the terms and conditions of the Creative Commons Attribution (CC BY) license (<https://creativecommons.org/licenses/by/4.0/>).

1. Introduction

Steel reinforcement is highly susceptible to rust in the chloride environment [1–5], which is an important issue that leads to the deterioration of the safety and durability of reinforced concrete structures in marine areas [6–8]. In recent years, the development of real estate in coastal areas has been extensive, and the shelving of the project schedule has led to severe corrosion of exposed steel reinforcement in foundation columns, shear walls, and post-cast belts [9–12]. Therefore, the protection of reinforced concrete structures is a critical issue that needs to be resolved urgently in our country's economic development. Traditional protection methods such as increasing the compactness and thickness of the concrete protective layer, coating anticorrosion coatings on the surface of the hardened concrete, and applying corrosion inhibitors can help prevent rusting of reinforcements [13–16]. Before implementing protective measures for reinforcement, the rusty surface of a corroded reinforcement needs to be removed. However, due to corroded reinforcements being located in the complicated and hidden regions of buildings, traditional mechanical and manual methods can hardly remove the rust layer on the reinforcement surface. In most previous studies [17–19], chemical converters were used to transform the active rusty layer of steel into an inert protective layer for anticorrosion.

The most studied rust layer conversion system is the phosphoric acid–tannic acid system, widely used in rust inhibitors and low surface rust coatings. Tannic acid is a macromolecular polyphenol compound [20,21]. As an essential component in rust converters or coatings, tannic acid has an excellent anticorrosion effect when the addition amount is 5–15 g/L [22–26]. The molecular structure of tannic acid contains multiple hydroxyl

groups, which can form a stable chelate with Fe^{3+} [27–30] and control the transformation of $\gamma\text{-FeOOH}$ crystal phase to Fe_3O_4 crystal phase in the rust layer [31–34]. Thereby, a tannic acid based rust converter can inhibit the electrochemical corrosion in corroded steel and improve the corrosion resistance of rusted steel. However, as tannic acid is a weak acid, the pH value significantly influences its molecular morphology and product structure in solution [35,36]. Winkelmann et al. [37] claimed that tannins accelerate the corrosion process by lowering the pH and forming complexes with iron that do not adhere to the surface. As a medium-strength acid, phosphoric acid has a more substantial acidity that can provide a suitable pH value for the rust converter [38]. Simultaneously, phosphoric acid and the steel substrate undergo a phosphating reaction to form a dense phosphating layer whose main component is FePO_4 [39–42], thus improving the corrosion resistance of the substrate. In the process of chemical interaction with the rust layer, phosphoric acid can convert the unstable rust layer into an ionic form so that a large number of hydroxyl groups contained in tannic acid are more likely to chelate with Fe^{3+} [43,44]. Therefore, the combination of phosphoric acid and tannic acid (PTA) rust converters can promote the conversion process of rust and significantly improve the corrosion resistance of steel [45–48].

In the rust conversion system, alcohol amine compounds often exist as organic corrosion inhibitors [49,50]. The use of alcohol amine compounds as corrosion inhibitors is related to the relative facility of introducing new functional groups in their structures and producing new compounds with high inhibitor efficiencies [51]. Furthermore, the adsorption of these compounds on the metallic surface can be done by physical or chemical adsorption, involving the electrostatic interaction between molecules and metal surface and also the charge sharing between the metal surface (d-orbital) and the heteroatoms and the aromatic ring of the organic molecules [52,53]. The formation of surface chelate is an essential reason for the corrosion inhibition effect of alcohol amine compounds [54,55]. Since the heteroatoms such as N and O in the alcohol amine compounds have different lone pairs of electrons, they can coordinate with the exposed iron atoms on the surface of the rusty steel or the Fe^{2+} in the hydroxide protective film, forming a chemical adsorption layer to achieve corrosion inhibition effect [56,57]. Besides, the H atom and O atom form an intermolecular hydrogen bond in the chelate unit structure, enhancing the stability of the hydroxide layer, thereby enhancing protection [58]. At the same time, the addition of alcohol amine compounds increases the alkalinity of the medium, which is conducive to the formation of hydroxide protective film, thus producing partial corrosion inhibition.

In our previous pre-experiment, adding different kinds and amounts of alcohol amines to the PTA-based rust converter significantly influenced the rust conversion of rusty steel. The selected four alcohol amine compounds mainly provide alkaline environment and polar adsorption groups and are used in conjunction with related weakly acidic PTA to achieve a synergistic protective effect. Among them, alcohol amine A has a hydroxyl substituent (-OH) on the main chain, alcohol amine B has two hydroxyl substituents (-OH) on the main chain, alcohol amine C has three hydroxyl substituents (-OH) on the main chain, and alcohol amine D has a hydroxyl substituent (-OH) and two methyl groups (- CH_3) on the main chain. The alkalinity of alcohol amine D is stronger than that of other alcohol amines. In addition, as the number of substituents increases, the basicity gradually decreases. From the perspective of the stability of ammonium cations, the more hydrogen bonds formed between alcohol amine and water, the more stable the ammonium cations formed, and the stronger the alkalinity.

In this study, in the first step, four different kinds of alcohol amines were used to modify the original PTA rust converter for obtaining the best rust conversion performance when applying on the rusty carbon steel. In the second step, the rust converter with the best performance was used to prepare the waterborne polymer-based rust conversion-based paints for rusty steel. An optimized preparation process is suggested for making the rust conversion-based paint with the best short-term and long-term anticorrosion and rust conversion performances.

2. Materials and Methods

2.1. Materials

Waterborne vinylidene chloride acrylic resin (56.8%) was purchased from Shanghai Yuanhe Chemical Co., Ltd. (Shanghai, China). Phosphoric acid (85%) was purchased from Tianmao Chemical Co., Ltd. (Xi'an, China). Tannic acid (81%) was purchased from Ding Shengxin Chemical Co., Ltd. (Tianjin, China). Alcohol amine A (99.9%), alcohol amine B (99%), alcohol amine C (99%), alcohol amine D (99.9%), copper sulfate, sodium chloride, hydrochloric acid were purchased from Xiaoshi Chemical Co., Ltd. (Ji'nan, China). Defoaming agent, moisture agent, and thickening agent were purchased from Wengjiang Chemical Reagent Co., Ltd. (Guangzhou, China). All reagents were of analytical grade unless otherwise stated. A Q235 carbon steel sheet, with dimensions of 120 mm × 50 mm × 0.5 mm, was exposed to the natural environment for two years. Carbon steel electrodes, with the size of ϕ 11 mm × 15 mm, were polished with sandpaper, cleaned with ethanol, and then immersed in the sodium chloride with a dosage of 3.5 wt.% for four weeks and exposed in the natural environment for another two weeks. The infrared spectra of the four alcohol amines are shown in Figure 1. The chemical composition of Q235 carbon steel is shown in Table 1. The natural environmental conditions of Q235 carbon steel exposure are shown in Table 2.

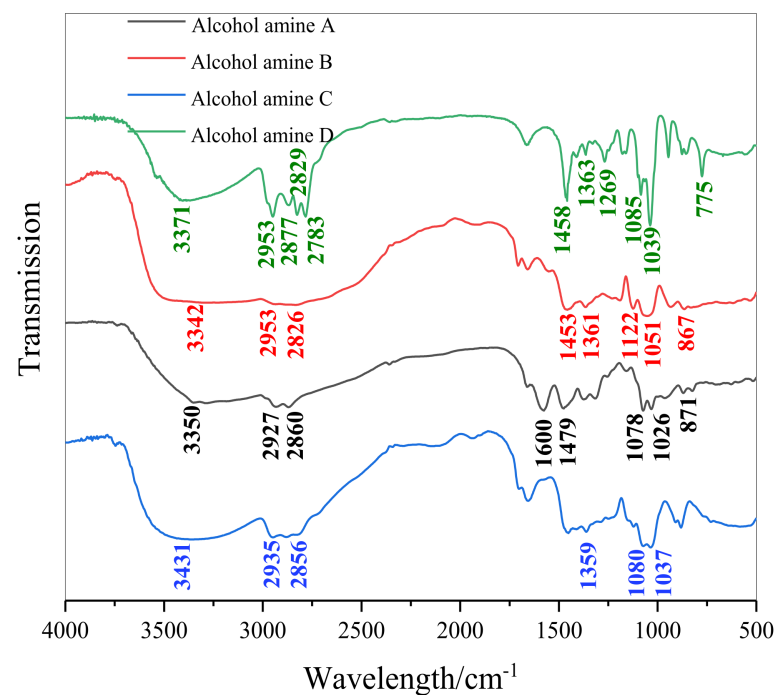


Figure 1. The infrared spectra of the four alcohol amines.

Table 1. The chemical composition of Q235 carbon steel (melting analysis).

Steel Grade	Quality Grade	Chemical Composition (%)							
		C	Si	Mn	S	P	Cr	Ni	Cu
Q235	B	0.200	0.350	1.400	0.030	≤ 0.030	0.30	0.30	0.20

Table 2. Environmental data of Q235 carbon steel exposure.

Location	Average Temperature (°C)	Relative Humidity (%)	Wetting Time (h/a)	Rainfall (mm/a)	Sunshine Time (h/a)	Cl ⁻ Deposition Rate (mg/100cm ² /d)	SO ₂ Deposition Rate (mg/100cm ² /day)	Rainwater (pH)
Yantai	11.8	68	4049	651.9	2698.4	0.250	1.184	6.1

2.2. Preparation of Waterborne Polymer-Based Paints

Tannic acid was dispersed into glycerol and stirred for 15 min to obtain the component A. Phosphoric acid was dispersed into the distilled water, and then penetrant agent, followed by stirring and mixing for 20 min to obtain the component B. At 60 °C, the components A and B were stirred at 3000 r/min for 20 min until well combined. Different formulations were prepared using four different amines as neutralizers to obtain the alcohol amine modified PTA rust converters named RC-A, RC-B, RC-C, and RC-D, respectively.

Then, the PTA rust converter with excellent performance was selected and added to the waterborne vinylidene chloride acrylic resin (VDC-MA) according to different proportions (0 wt.%, 5 wt.%, 10 wt.%, 15 wt.%, 20 wt.%), supplemented with the defoaming agent, moisture agent, and thickening agent to obtain the waterborne polymer-based paints. The detailed mass ratios between ingredients are shown in Table 3.

Table 3. The mass ratios of ingredients in waterborne polymer-based paints.

Group	Alcohol Amine Modified PTA Rust Converter	VDC-MA	Defoaming Agent	Moisture Agent	Thickening Agent
1#	0 wt.%	1	1‰	1‰	1‰
2#	5 wt.%	1	1‰	1‰	1‰
3#	10 wt.%	1	1‰	1‰	1‰
4#	15 wt.%	1	1‰	1‰	1‰
5#	20 wt.%	1	1‰	1‰	1‰

2.3. Characterization

2.3.1. Surface Observation

The surface topography of the rusty steel surface was observed by Olympus DSX1000 digital microscope (Shanghai Cinv Optical Technology Co., Ltd., Shanghai, China).

The FTIR spectra were obtained using an Irtfinity-1s FT-IR spectrometer (SHIMADZU, Kyoto, Japan) at room temperature.

2.3.2. Rust Conversion Performance

The copper sulfate drop test and 3.5 wt.% NaCl solution immersion test were used to measure the rust conversion ability of amine-modified rust converters at 20 °C. The copper sulfate dropping experiment's method was as follows: Rust reformer was evenly brushed on the rusty steel sheets, and a drop of copper sulfate solution was dropped on the dry rust converter film. At the same time, a stopwatch was started to observe the time when the liquid drops change from sky blue to light yellow or light red, which was marked as T_{red} . The NaCl solution immersion test operation was as follows: The rust converters were evenly brushed on the rusty steel sheets; after the film was dried, the coated steel plate was put into 3.5 wt.% NaCl solution to soak, and the time of rust spots appearing on the surface of the steel plates was recorded and marked as $T_{reccorr}$.

During the soaking test, the concentration of a ferric ion in the soak solution was measured by METASH UV-8000 spectrometer (Shanghai METASH instruments Co., Ltd., Shanghai, China) after soaking of 24, 48, and 72 h. For the same steel sheet immersion solution, three groups of samples were taken to test the ferric ion concentration, and the average value of the three tests was the iron ion concentration value in the immersion solution.

2.3.3. Basic Properties and Antipeeling Performance

The impact resistance of the polymer-based paint was tested by ASTM D2794-1993, the bending performance was tested by ISO 1519-2002, the pencil hardness was tested following ASTM D3363-2005, and the peel resistance was tested by ASTM D3359-2009. The tensile property of the polymer-based paint film was tested by the SMT-5000 Universal Testing Machine (Seth Testing Equipment Co., Ltd., Zhejiang, China), which was tested in accordance with ASTM D882-2010. The adhesive force was determined using PosiTest AT-ATM20A adhesion tester (DeFeLsko Inspection instruments, Ogdensburg, NY, USA) with a stand-off size of 20 mm.

2.3.4. Swelling Degree and Water Contact Angle Measurement

The polymer-based paint films were placed at room temperature for 7 days, and the water contact angle was measured by a POAREACH JC2000D (Zhongchen Digital Technology Equipment Co., Ltd., Hong Kong, China). The prepared films were then cut into pieces with a size of 3 cm × 1 cm and heated in an oven at 50 °C for 24 h to remove the residual solvent. At 25 °C, the samples were placed in DMF (N,N-dimethylformamide) for 10 min and then taken out, and the surface solvent was dried with filter paper and weighed until the sample quality remained unchanged. The swelling degree of samples was calculated according to the following equation:

$$Q = (m_d - m_0) / m_0 \quad (1)$$

where Q is swelling degree of coating and m_0 and m_d are the mass of the sample before swelling and after swelling equilibrium, respectively.

2.3.5. Anticorrosion Performance

The carbon steel samples coated with polymer-based paints were immersed in 50 g/L sulfuric acid solution, 50 g/L sodium hydroxide solution, and 35 g/L sodium chloride solution to test acid resistance, alkali resistance, and salt resistance by recording the surface states of carbon steel every 24 h.

A PARSTAT2273 electrochemical workstation (Princeton Applied Research, Oak Ridge, TN, USA) was used to measure the electrochemical impedance spectra (EIS) and the linear polarization resistance (LPR) of rusty steel electrodes. A three-electrode system was used with rusty steel electrodes in 3.5 wt.% NaCl solution as working electrodes, the saturated calomel electrode as the reference electrode, and the platinum electrode as the auxiliary electrode to evaluate the anticorrosion properties of PTA rust converters and waterborne polymer-based paints. The effective working area was 1 cm², the test frequency was in the range of 0.01 Hz to 10 kHz, and the excitation signal was 5 mV.

3. Results and Discussion

3.1. Rust Conversion Capacity of PTA Rust Converters

3.1.1. Optical Surface Topography Analysis

The diagrams of the surface morphology, 3D morphology, and section morphology of rusted carbon steel sheets treated with different composite PTA rust converters are shown in Figure 2. The rust layer of the untreated sample has a thick grain and loose structure. The section morphology can be divided into the brownish-red rusty layer and the steel matrix layer. The surface roughness of the corroded steel plate after the compound rust converter treatment is reduced, and the rusty layer is converted into the continuous smooth and dense passivation film layer. Among the four rust converter treated rusty carbon steel sheets, the passivation film roughness and density of the steel surface treated with RC-D are the lowest and the best. Thus, it can be speculated that the corrosion resistance and antipeeling performances of the RC-D are the best. The following sections discuss the anticorrosion and antipeeling properties of rusty steel sheets treated with each composite rust converter to verify this speculation.

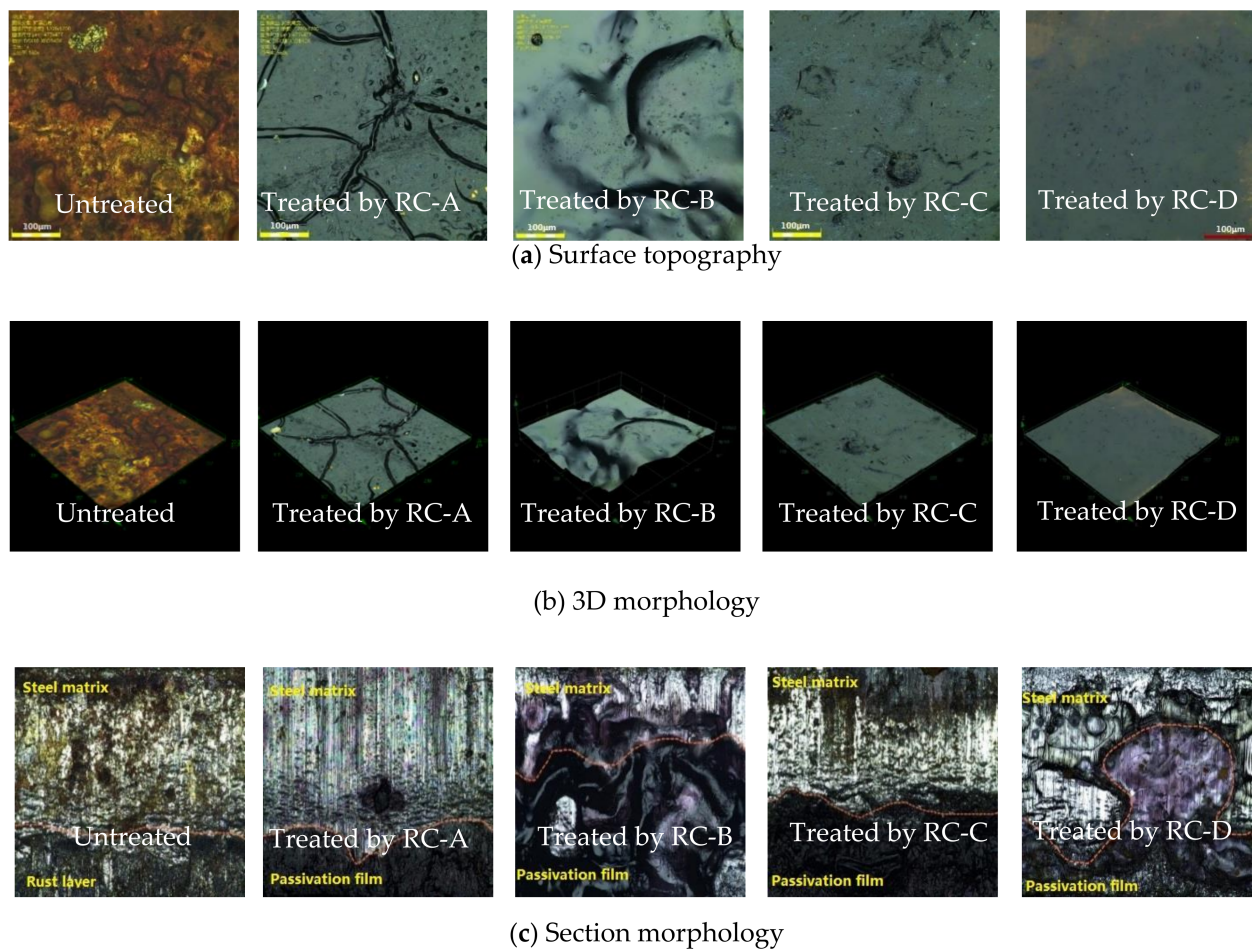


Figure 2. Morphology of rusty steel sheets treated with RC-A, RC-B, RC-C, and RC-D ($\times 560$).

3.1.2. Anticorrosion Property Analysis

The T_{red} and T_{recurr} curves of the rusty carbon steel sheets treated with different compound rust converters are shown in Figure 3. The T_{red} values of RC-A, RC-B, RC-C, and RC-D are 172, 204, 230, and 251 s, respectively; the T_{recurr} values of RC-A, RC-B, RC-C, and RC-D are 130, 160, 180, and 210 s respectively. The concentration of Fe^{3+} of rusty carbon steel plates treated with different compound PTA rust converters in the soaking solution is shown in Figure 4. The concentration of Fe^{3+} dissolved on the surface of rusty carbon steel treated with RC-A, RC-B, RC-C, and RC-D first decreased and then increased. Compared with the experimental group, Fe^{3+} on the surface of the blank rusty carbon steel plate was precipitated in a large amount after 48 h of soaking. These results indicate that treatment with RC-A, RC-B, RC-C, and RC-D reduces the concentration of Fe^{3+} dissolved on the surface of rusted carbon steel, playing an excellent protective role on the rusty carbon steel sheet. Within 72 h of soaking, the concentration of Fe^{3+} in the soaking solution of rusty carbon steel treated with RC-D was the lowest. As a result, the RC-D showed the best rusty conversion performance when applied on the rusty carbon steel sheet in this study. The main reason is that the alkalinity of alcohol amine D is stronger than that of other alcohol amine compounds, which is beneficial to the formation of the hydroxide protective film. At the same time, the number of H atoms and O atoms in the alcohol amine D is greater, which is more conducive to the formation of intermolecular hydrogen bonds in the structure of the chelating unit, which enhances the stability of the hydroxide layer, thereby playing a corrosion inhibition role [56–58].

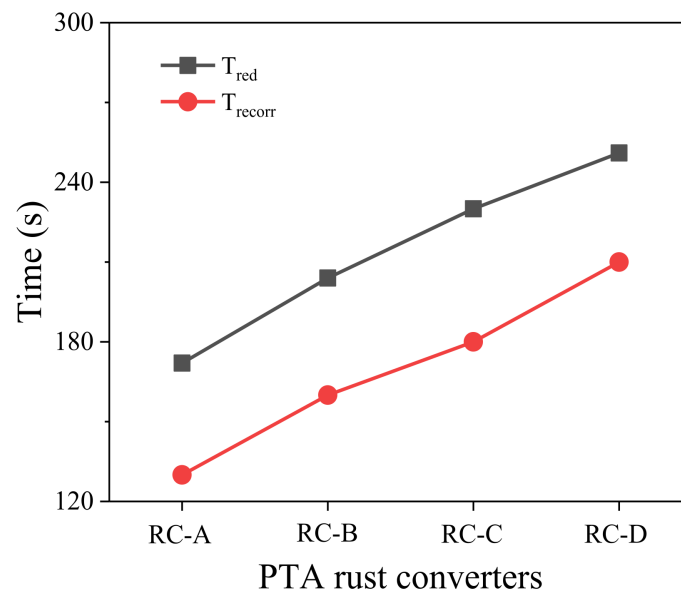


Figure 3. The T_{red} and T_{recorr} curves of rusty steel sheets treated with RC-A, RC-B, RC-C, and RC-D.

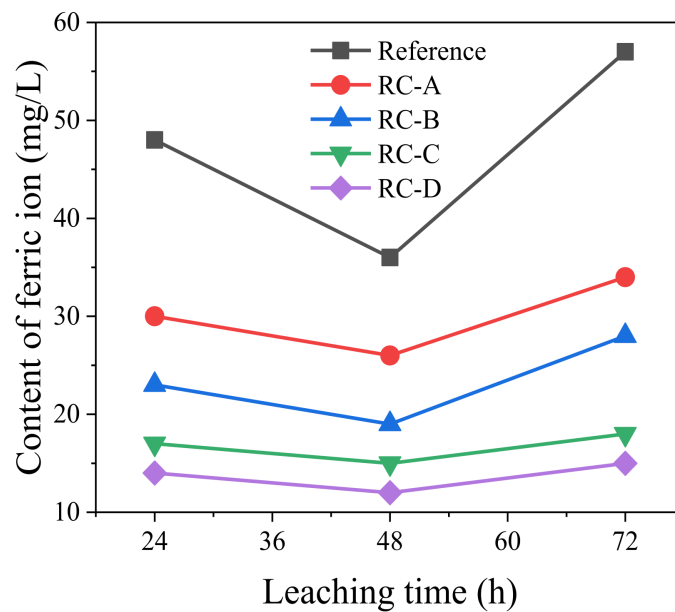


Figure 4. The Fe^{3+} concentration of rusty steel sheets treated with RC-A, RC-B, RC-C, and RC-D at different immersion times.

EIS images of rusty carbon steel electrodes treated with different compound rust converters are shown in Figure 5. The highest phase angle in the low-frequency zone of the rusty work electrodes treated with RC-A, RC-B, RC-C, and RC-D is higher than 60 degrees. After RC-D treatment, the low-frequency zone phase angle of the rusty steel electrode is highest, and the radius of the impedance frequency response plot is the largest. The results of electrochemical impedance spectroscopy also indicate that the anticorrosion of RC-D-treated electrode is the best.

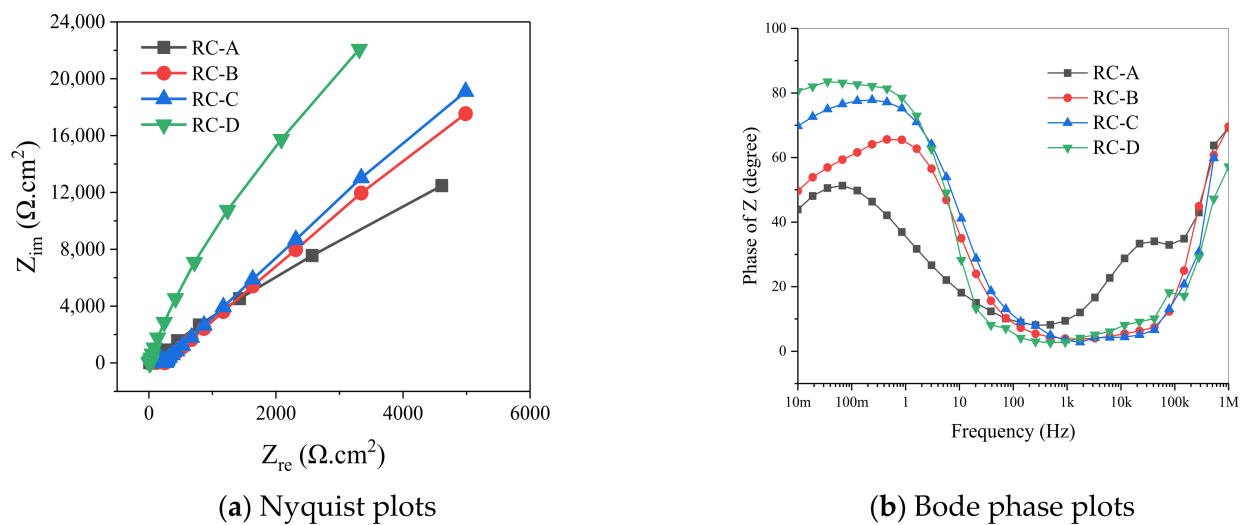


Figure 5. EIS of rusty steel electrodes treated with RC-A, RC-B, RC-C, and RC-D.

3.1.3. Antipeeling Property Analysis

The adhesive strength and failure status after rusty steel sheets treat by RC-A, RC-B, RC-C and RC-D, as shown in Figure 6. The rust layer of untreated carbon steel is mainly composed of Fe_3O_4 , $\alpha\text{-FeOOH}$ and $\gamma\text{-FeOOH}$. The structure is loose and the adhesion strength is only 0.61 MPa. When it peels off, it shows the damage between the rust layer and the metal matrix.

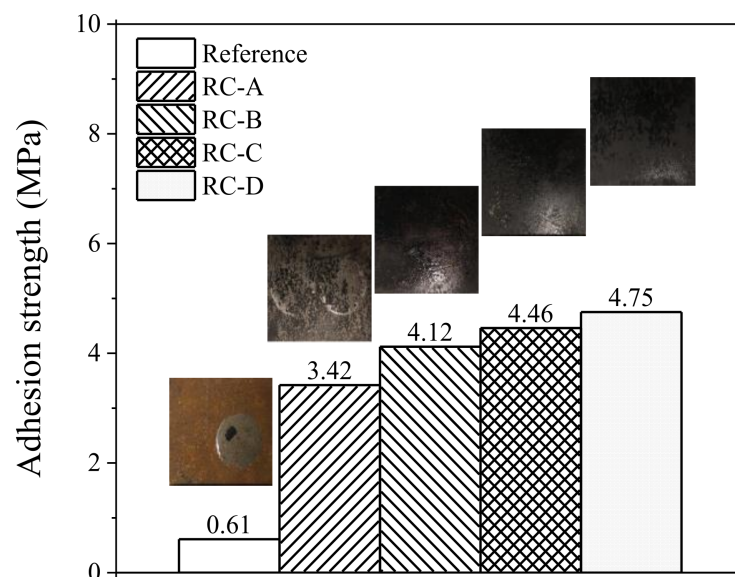


Figure 6. The adhesive strength and the failure status between passivation film and rusty steel.

After RC-A, RC-B, RC-C, and RC-D treatment, the adhesive strength between the surface layer and the rusty carbon steel increase by 5.6 times (RC-A), 6.8 times (RC-B), 7.3 times (RC-C), and 7.8 times (RC-D) of the untreated one. Moreover, the peeling manifests as the destruction of the epoxy adhesive and the metal substrate the passivation film, indicating the rust converters have excellent adhesion on the rusty steel sheet surface. Among them, the adhesion force of the corroded steel plate after RC-D treatment is up to 4.75 MPa. The main reason is that the rust layer is transformed into a thick passivation film whose main components are insoluble substances such as iron tannate chelate and iron phosphate [28,30], and the hydroxyl group in iron tannate chelate can adsorb the metal matrix, thereby improving the adhesion of the corroded steel plate [43,44].

3.1.4. Surface Chemical Composition Analysis

Representative FT-IR spectra of untreated and RC-A-, RC-B-, RC-C-, and RC-D-treated carbon steel are shown in Figure 7. In the spectrum of untreated rusty steel, the characteristic absorption peaks of Fe_3O_4 are observed at 630 and 550 cm^{-1} , which can be ascribed to the vibrations of the Fe-O group [59–61]. The bands at 792 and 892 cm^{-1} were ascribed to the Fe-OH-Fe bending vibrations of $\alpha\text{-FeOOH}$ [62]. The diagnostic absorption bands of $\gamma\text{-FeOOH}$ appeared at 1156 and 1022 cm^{-1} for the in-plane and 745 cm^{-1} for the out-of-plane Fe-OH bending vibrations [63,64]. There are apparent absorption peaks at 3111 and 3420 cm^{-1} , corresponding to the absorbed H_2O molecule or Fe-OH vibration. The band at 1630 cm^{-1} was assigned to H_2O bending vibrations. These results support the conjecture in Section 3.1.3. The surface rust layer of carbon steel is mainly composed of Fe_3O_4 , $\alpha\text{-FeOOH}$, and $\gamma\text{-FeOOH}$, which have loose structures, leading to low adhesion.

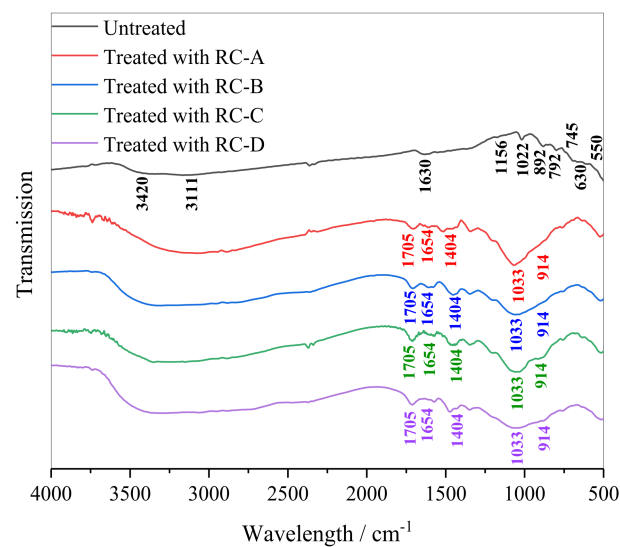


Figure 7. FT-IR spectra of untreated rusty steel sheet and steel sheet treated with RC-A, RC-B, RC-C, and RC-D.

In the FTIR spectrum of rusty carbon steel sheet treated with RC-A, RC-B, RC-C, and RC-D, the absorption peaks of 1705 , 1654 , and 1404 cm^{-1} correspond to the aromatic ring absorption peak of tannic acid, the absorption peak of 914 cm^{-1} is the chelate absorption peak of iron tannate, and the sharp absorption peak of P-O bond stretching vibration of PO_4^{3-} is at 1033 cm^{-1} . The above results prove that RC-A, RC-B, RC-C, and RC-D can transform steel rust into iron phosphate and iron tannate chelates. These results also support the conjecture in Section 3.1.1; the rust layer of the tested rusty steel sheet has transformed into iron phosphate and iron tannate chelates, forming a compact and smooth protective layer.

3.2. Properties of Waterborne Polymer-Based Paints

From the above performance test results of alcohol amine modified PTA rust converters, it can be seen that the characterization of RC-D is relatively excellent. Therefore, different ratios of RC-D were added to VDC-MA to prepare waterborne polymer-based paints, and their performance was characterized.

3.2.1. Basic Mechanical Properties

The basic physical properties of the waterborne polymer-based paints are listed in Table 4. With the addition of RC-D, the toughness of VDC-MA increases, further increasing the flexural resistance and impact toughness of the paint film. Adding an appropriate amount of RC-D can dissolve the rust layer and transform it into iron tannate and other chelate compounds to act as filler, thus enhancing the adhesion between the paint film and

the metal matrix. However, when the amount of RC-D is higher than 10 wt.%, the adhesion level of paint film remains unchanged.

Table 4. Basic physical properties table of waterborne polymer-based paints.

Paints Code	Add Amount	Impact Resistance (100 cm)	Bending Property (2 mm)	Cross-Hatch Adhesion	Pencil Hardness
1#	0 wt.%	Failed	Failed	3	2H
2#	5 wt.%	Pass	Pass	1	2H
3#	10 wt.%	Pass	Pass	0	2H
4#	15 wt.%	Pass	Pass	0	2H
5#	20 wt.%	Pass	Pass	0	2H

3.2.2. Swelling Degree and Water Contact Angle Analysis

The swelling degrees and water contact angles of polymer-based paint films with different amounts of RC-D are shown in Figure 8. The swelling degree of waterborne VDC-MA film is 6.5%. As the amount of RC-D increases, the swelling degree of the polymer-based paint films shows an upward trend, indicating that the presence of RC-D reduces the crosslinking density of composite-based paint films. On the one hand, this may be because the boiling point of the solvent in RC-D is higher than the film formation temperature, and it is not completely volatilized. On the other hand, it may be because the rust layer is dissolved and converted into chelate such as iron tannate, which, as filler, reduces the crosslinking density of the coating, leading to an increase in the swelling degree [27,32]. As shown in Figure 8, the water contact angle of the VDC-MA film itself is 54.36°. The water contact angles of polymer-based paint films decrease with the increase in RC-D content, mainly because there are more hydrophilic groups in RC-D, which enhances the hydrophilicity of the polymer-based paint films, resulting in a decrease in the water contact angle.

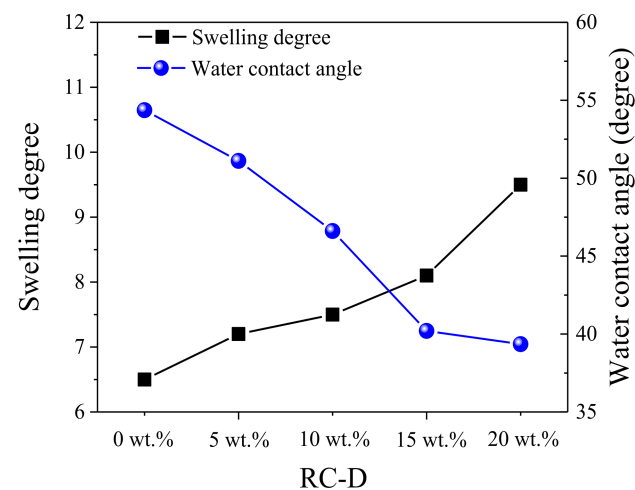


Figure 8. The swelling degrees and water contact angles of polymer-based paint films.

3.2.3. Tensile and Antipeeling Property Analysis

The stress–strain curves of five paint films during the tensile process are shown in Figure 9, and the tensile strength of the VDC-MA film itself is 32 MPa. The tensile strength of the polymer-based paint film decreases with the increase in RC-D content, while the elongation at break increases. According to the crosslinking degree test results in Section 3.2.2, the existence of RC-D reduces the crosslinking density of the composite-based paints. As a result, the amount of RC-D should not be too large.

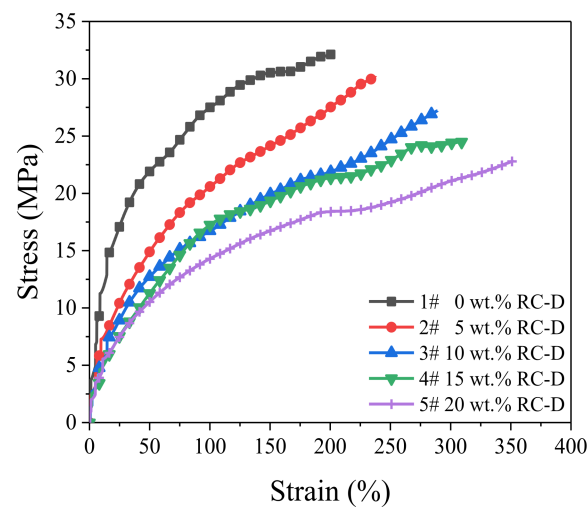


Figure 9. The stress–strain curves of five polymer-based paint films.

The adhesive strength between the polymer-based paint film and the rusty carbon steel sheets and the failure types in the surface peeling tests are shown in Figure 10. Before RC-D was added, the adhesion of VDC-MA coating film was low, only 1.03 MPa. The main reason is that the rust layer does not dissolve after coating with VDC-MA, and the polar groups in VDC-MA cannot be directly adsorbed on the rusted steel sheet surface. With the increase in the RC-D content, the adhesion of the coating film increased first and then decreased. This is mainly because after adding RC-D, the polymer-based material can dissolve the rust layer to form a chelate, thereby filling the gap, so that the polar groups in the polymer-based material are directly adsorbed on the metal substrate surface, and the adhesion is significantly improved [27,52,53]. However, when the RC-D content is too large, the cross-linking density of VDC-MA will be significantly reduced, resulting in a decrease in the continuity and adhesion of the coating film. When the RC-D to VDC-MA ratio is 10 wt.%, the rust layer can be completely dissolved and transformed into fillers, leading to the highest adhesive strength of 3.06 MPa.

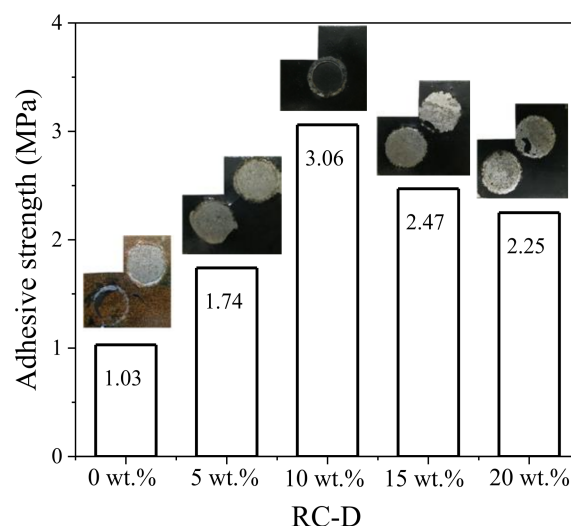


Figure 10. The adhesive strength between each polymer-based paint film and the rusty carbon steel sheets and the failure types in the surface peeling tests.

3.2.4. Optical Surface Topography

Figures 11 and 12 show the microscopic morphology of the rusted steel sheets coated with waterborne VDC-MA and the composite-based paint (RC-D:VDC-MA = 10 wt.%). As shown in Figure 11a, the waterborne VDC-MA is transparent after curing, and the

brownish-red rust layer on the steel sheet surface is relatively apparent, indicating the waterborne VDC-MA cannot react with rust. In Figure 11b, the steel sheet's cross-section morphology shows a relatively visible three-layer structure, namely the underlying metal matrix, the middle rust layer, and the VDC-MA coating on the surface. As shown in Figure 11c, the surface roughness of the steel sheet coated with waterborne VDC-MA is very high. Since there are many granular projections in the rust layer, the VDC-MA film cannot be evenly distributed on the rusty steel sheet surface.

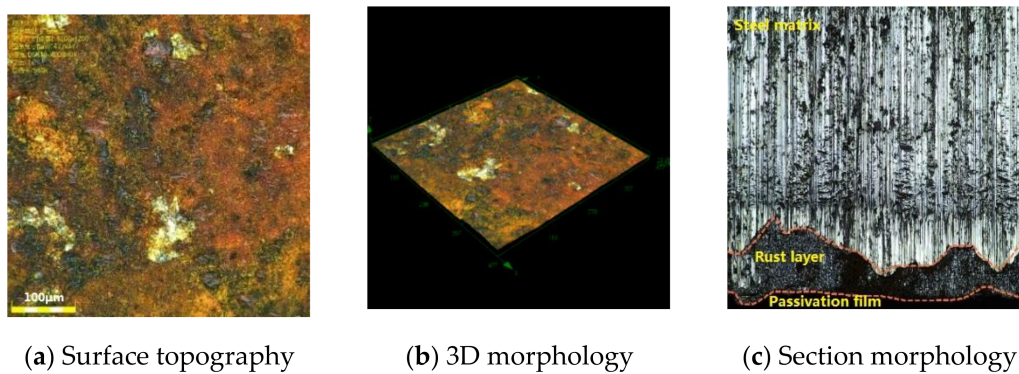


Figure 11. Morphology of rusty steel plate coated with water VDC-MA film ($\times 560$).

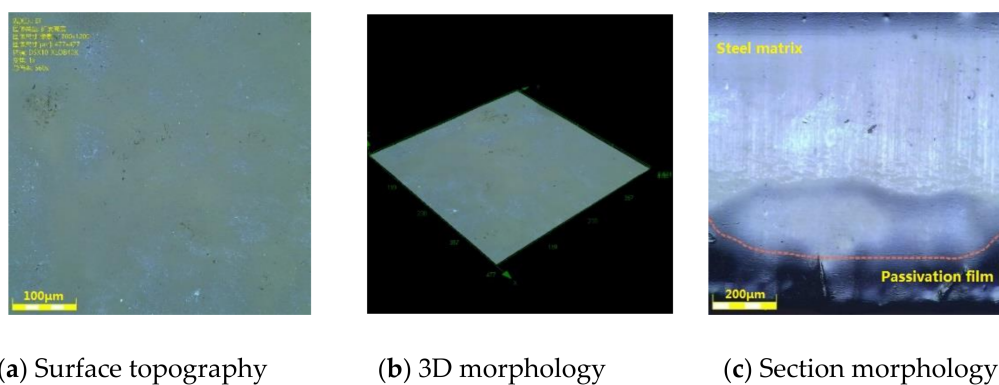


Figure 12. Morphology of rusty steel plate coated with composite-based paint film with the RC-D to VDC-MA ratio of 10 wt.% ($\times 560$).

In Figure 12a, the typical blue-black iron tannate is observed in the surface layer of the rusty steel sheet coated with the composite-based paint, while the brownish-red iron layer is not observed, which confirms that the tannic acid components in the rust converter had reacted with the rust to form iron tannate. In Figure 12b, the steel sheet's cross-section morphology shows a typical double-layer structure, namely the metal substrate at the bottom and the composite-based paint layer at the top, which confirms that the original rust layer of the rusty steel sheet has been completely transformed into iron tannate. Therefore, in Figure 12c, no granular convex is seen in the three-dimensional morphology diagram of the steel sheet, and the surface roughness is relatively low.

3.3. Long-Term Anticorrosion Performance of Waterborne Polymer-Based Paints

The variation curves of polarization resistance (R_p) and corrosion current density (I_{corr}) of different polymer-based coatings are shown in Figure 13. As the immersion time increases, the R_p of the VDC-MA coating continues to decrease, and I_{corr} continues to increase. After immersing for three days, the I_{corr} of the VDC-MA coating exceeds $0.01 \mu\text{A}/\text{cm}^2$, indicating that the electrode has been corroded. After adding RC-D, the R_p of the polymer-based coating is significantly increased and I_{corr} is reduced. When the addition amount of RC-D is 10 wt.%, the I_{corr} of the polymer-based coatings rises steadily

within 30 days, and the I_{corr} is $0.003 \mu\text{A}/\text{cm}^2$ on the 30th day, which is much less than $0.1 \mu\text{A}/\text{cm}^2$, and the corrosion resistance is the best.

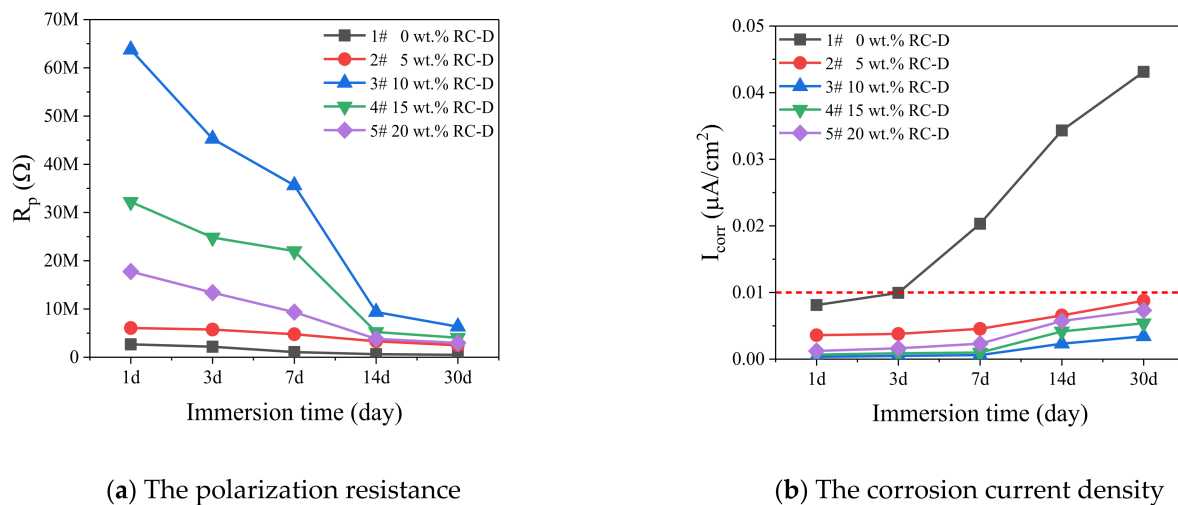


Figure 13. R_p and I_{corr} of different polymer-based coatings.

The acid resistance, alkali resistance, and salt resistance of different polymer-based coatings are shown in Table 5. After being immersed in sulfuric acid solution for 14 days, the rust layer on the steel plate coated with VDC-MA has not been transformed, and the bonding force between the coating and the steel plate is weak. Corrosive media can easily penetrate into the coating and cause corrosion of the steel plate. The ability to withstand acids, alkalis, and salts is poor. After adding RC-D, the coating exhibits good acid, alkali, and salt resistance. When the addition amount of RC-D is 10 wt.%, there is no blistering or cracking on the coating surface, which is consistent with the electrochemical test results.

Table 5. The acid resistance, alkali resistance, and salt resistance of different polymer-based coatings.

Paints Code	Add Amount	Acid Resistance (14 Days)	Alkali Resistance (28 Days)	Salt Resistance (30 Days)
1#	0 wt.%	Blistering	Rusty	Rusty
2#	5 wt.%	Unchanged	Unchanged	Rusty
3#	10 wt.%	Unchanged	Unchanged	Unchanged
4#	15 wt.%	Unchanged	Unchanged	Unchanged
5#	20 wt.%	Unchanged	Unchanged	Unchanged

According to the results in Section 3.2.2, the RC-D can transform iron rust into iron tannate, making a denser and stable protective layer on the surface of the original steel sheet. As shown in Table 5, when the RC-D to VDC-MA mass ratio is higher than 10 wt.%, the coated rusty steel sheets show good acid, alkali, and salt resistances. These results prove that this protective layer has excellent acid, alkali, and salt resistances.

4. Conclusions

This work studied the rust layer structure and rust conversion capacity of different alcohol amine adjusted PTA rust converters. The effects of different alcohol amine modified PTA rust converters on the basic mechanical properties, optical surface topography, and antistripping properties of the waterborne composite-based paints were analyzed. Moreover, the long-term anticorrosion performance of polymer composite-based paint was tested by electrochemical testing methods. The following conclusions can be drawn:

(1) After treatment with RC-D, the passivation film observed on the original rusty steel surface becomes the smoothest and densest. Besides, the RC-D rust converter shows the best anticorrosion and antipeeling properties.

(2) The RC-D can convert the rust layer into a flat and dense protective film with iron tannate and iron phosphate as the main components, reducing the leaching of Fe^{3+} on the steel surface. Thus, the alcohol amine D significantly improved the rust conversion capacity and anticorrosion performances of the PTA rust converter.

(3) The mass ratio of RC-D and VDC-MA influences the mechanical and anticorrosion properties of the paints. When RC-D to VDC-MA mass ratio is 10 wt.% in the composite-based paint, the rust layer on the surface of the rusty carbon steel is wholly converted into a blue-black and relatively flat passivation film, and the composite-based paint obtains suitable swelling degree and water contact angle. As a result, the composite-based paint containing 10 wt.% RC-D shows the best tensile, antipeeling, and long-term anticorrosion performances when painted on the rusty surface of carbon steel.

Author Contributions: Data curation, Y.C.; writing—original draft, Y.C.; investigation, S.L.; formulation of overarching research goals, funding, supervision, Z.L.; literature search, data interpretation, Z.W. All authors have read and agreed to the published version of the manuscript.

Funding: The study was supported by the Key Projects of Shandong Natural Science Foundation (grant number ZR2020KE049), the National Natural Science Foundation of China (grant numbers 51678512 and 51278443), and the Research and Development Key Project of Shandong Province (grant number 2017GGX70107).

Institutional Review Board Statement: Not applicable.

Informed Consent Statement: Not applicable.

Data Availability Statement: Data are contained within the current manuscript.

Conflicts of Interest: The authors declare that they have no known competing financial interest or personal relationships that could have appeared to influence the work reported in this paper.

References

- Zhang, S.; Hou, L.; Du, H.; Wei, H.; Liu, B.; Wei, Y. A study on the interaction between chloride ions and CO_2 towards carbon steel corrosion. *Corros. Sci.* **2020**, *167*, 108531. [[CrossRef](#)]
- Berrolcal, C.G.; Lundgren, K.; Löfgren, I. Corrosion of steel bars embedded in fibre reinforced concrete under chloride attack: State of the art. *Cem. Concr. Res.* **2016**, *80*, 69–85. [[CrossRef](#)]
- Stefanoni, M.; Angst, U.; Elsener, B. Corrosion rate of carbon steel in carbonated concrete—A critical review. *Cem. Concr. Res.* **2018**, *103*, 35–48. [[CrossRef](#)]
- Cao, Y.; Gehlen, C.; Angst, U.; Wang, L.; Wang, Z.; Yao, Y. Critical chloride content in reinforced concrete—An updated review considering Chinese experience. *Cem. Concr. Res.* **2019**, *117*, 58–68. [[CrossRef](#)]
- Zhu, W.; François, R.; Zhang, C.; Zhang, D. Propagation of corrosion-induced cracks of the RC beam exposed to marine environment under sustained load for a period of 26 years. *Cem. Concr. Res.* **2018**, *103*, 66–76. [[CrossRef](#)]
- Xu, F.; Xiao, Y.; Wang, S.; Li, W.; Liu, W.; Du, D. Numerical model for corrosion rate of steel reinforcement in cracked reinforced concrete structure. *Constr. Build. Mater.* **2018**, *180*, 55–67. [[CrossRef](#)]
- Yang, H.; Li, W.; Liu, X.; Liu, A.; Hang, P.; Ding, R.; Li, T.; Zhang, Y.; Wang, W.; Xiong, C. Preparation of corrosion inhibitor loaded zeolites and corrosion resistance of carbon steel in simulated concrete pore solution. *Constr. Build. Mater.* **2019**, *225*, 90–98. [[CrossRef](#)]
- Jin, Z.; Zhao, X.; Zhao, T.; Li, J. Chloride ions transportation behavior and binding capacity of concrete exposed to different marine corrosion zones. *Constr. Build. Mater.* **2018**, *177*, 170–183. [[CrossRef](#)]
- Sun, C.; Yuan, L.; Zhai, X.; Qu, F.; Li, Y.; Hou, B. Numerical and experimental study of moisture and chloride transport in unsaturated concrete. *Constr. Build. Mater.* **2018**, *189*, 1067–1075. [[CrossRef](#)]
- Ye, H.; Tian, Y.; Jin, N.; Jin, X.; Fu, C. Influence of cracking on chloride diffusivity and moisture influential depth in concrete subjected to simulated environmental conditions. *Constr. Build. Mater.* **2013**, *47*, 66–79. [[CrossRef](#)]
- Huang, D.; Wei, J.; Liu, X.; Du, Y.; Zhang, S. Experimental study on influence of post-pouring joint on long-term performance of steel-concrete composite beam. *Eng. Struct.* **2019**, *186*, 121–130. [[CrossRef](#)]
- Cheewaket, T.; Jaturapitakkul, C.; Chalee, W. Initial corrosion presented by chloride threshold penetration of concrete up to 10 year-results under marine site. *Constr. Build. Mater.* **2012**, *37*, 693–698. [[CrossRef](#)]

13. Liu, Q.; Song, Z.; Han, H.; Donkor, S.; Jiang, L.; Wang, W.; Chu, H. A novel green reinforcement corrosion inhibitor extracted from waste *Platanus acerifolia* leaves. *Constr. Build. Mater.* **2020**, *260*, 119695. [[CrossRef](#)]
14. Li, M.; Liu, Z.; Yang, Z.; Wang, Z.; Yuan, H. Bond-slip behaviors between reinforced concrete and coated rebar via a new strain monitoring method and FEA simulation. *Constr. Build. Mater.* **2020**, 120402. [[CrossRef](#)]
15. Wang, P.; Wang, Y.; Zhao, T.; Xiong, C.; Xu, P.; Zhou, J.; Fan, Z. Effectiveness protection performance of an internal blending organic corrosion inhibitor for carbon steel in chloride contaminated simulated concrete pore solution. *J. Adv. Concr. Technol.* **2020**, *18*, 116–128. [[CrossRef](#)]
16. Song, Z.; Jiang, L.; Li, W.; Xiong, C.; Chu, H. Impact of compressive fatigue on chloride diffusion coefficient in OPC concrete: An analysis using EIS method. *Constr. Build. Mater.* **2016**, *113*, 712–720. [[CrossRef](#)]
17. Barrero, C.A.; Ocampo, L.M.; Arroyave, C.E. Possible improvements in the action of some rust converters. *Corros. Sci.* **2001**, *43*, 1003–1018. [[CrossRef](#)]
18. Li, R.; Yu, Q.; Yang, C.; Chen, H.; Xie, G.; Guo, J. Innovative cleaner production for steel phosphorization using Zn-Mn phosphating solution. *J. Clean. Prod.* **2010**, *18*, 1040–1044. [[CrossRef](#)]
19. Lin, B.; Lu, J.; Kong, G. Synergistic corrosion protection for galvanized steel by phosphating and sodium silicate post-sealing. *Surf. Coat. Technol.* **2008**, *202*, 1831–1838. [[CrossRef](#)]
20. Song, B.; Yang, L.; Han, L.; Jia, L. Metal ion-chelated tannic acid coating for hemostatic dressing. *Materials* **2019**, *12*, 1803. [[CrossRef](#)]
21. Wei, S.; Lin, Y.; Liao, M.; Zhou, H.; Li, Y. Characterization and antioxidative properties of condensed tannins from the mangrove plant *Aegiceras corniculatum*. *J. Appl. Polym. Sci.* **2012**, *124*, 2463–2472. [[CrossRef](#)]
22. Xu, W.; Han, E.; Wang, Z. Effect of tannic acid on corrosion behavior of carbon steel in NaCl solution. *J. Mater. Sci. Technol.* **2019**, *35*, 64–75. [[CrossRef](#)]
23. Zhang, S.F.; Zhang, R.F.; Li, W.K.; Li, M.S.; Yang, G.L. Effects of tannic acid on properties of anodic coatings obtained by micro arc oxidation on AZ91 magnesium alloy. *Surf. Coat. Technol.* **2012**, *207*, 170–176. [[CrossRef](#)]
24. Yang, J.; Wang, L.; Xie, A.; Dai, X.; Yan, Y.; Dai, J. Facile surface coating of metal-tannin complex onto PVDF membrane with underwater superoleophobicity for oil-water emulsion separation. *Surf. Coat. Technol.* **2020**, *389*, 125630. [[CrossRef](#)]
25. Chen, X.; Li, G.; Lian, J.; Jiang, Q. Study of the formation and growth of tannic acid based conversion coating on AZ91D magnesium alloy. *Surf. Coat. Technol.* **2009**, *204*, 736–747. [[CrossRef](#)]
26. Hoffmann, K.; Stratmann, M. The delamination of organic coatings from rusty steel substrates. *Corros. Sci.* **1993**, *34*, 1625–1645. [[CrossRef](#)]
27. Yang, W.; Sousa, A.M.M.; Thomas-Gahring, A.; Fan, X.; Jin, T.; Li, X.; Tomasula, P.M.; Liu, L. Electrospun polymer nanofibers reinforced by tannic acid/Fe⁺⁺⁺ complexes. *Materials* **2016**, *9*, 757. [[CrossRef](#)]
28. Singh, D.; Yadav, S. Role of tannic acid based rust converter on formation of passive film on zinc rich coating exposed in simulated concrete pore solution. *Surf. Coat. Technol.* **2008**, *202*, 1526–1542. [[CrossRef](#)]
29. Qian, B.; Hou, B.; Zheng, M. The inhibition effect of tannic acid on mild steel corrosion in seawater wet/dry cyclic conditions. *Corros. Sci.* **2013**, *72*, 1–9. [[CrossRef](#)]
30. Jain, R.; Sharma, A.; Bhadu, M.K.; Swarnkar, K. Synthesis of phosphorylated rust metamorphoses and its comparative corrosion study on steel samples simulated in different atmospheres. *Anti Corros. Methods Mater.* **2016**, *63*, 316–326. [[CrossRef](#)]
31. Nasrazadani, S. The application of infrared spectroscopy to a study of phosphoric and tannic acids interactions with magnetite (Fe₃O₄), goethite (α-FeOOH) and lepidocrocite (γ-FeOOH). *Corros. Sci.* **1997**, *39*, 1845–1859. [[CrossRef](#)]
32. Tan, K.W.; Kassim, M.J.; Oo, C.W. Possible improvement of catechin as corrosion inhibitor in acidic medium. *Corros. Sci.* **2012**, *65*, 152–162. [[CrossRef](#)]
33. Rahim, A.A.; Rocca, E.; Steinmetz, J.; Kassim, M.J. Inhibitive action of mangrove tannins and phosphoric acid on pre-rusted steel via electrochemical methods. *Corros. Sci.* **2008**, *50*, 1546–1550. [[CrossRef](#)]
34. Behpour, M.; Ghoreishi, S.M.; Khayatkashani, M.; Soltani, N. Green approach to corrosion inhibition of mild steel in two acidic solutions by the extract of punica granatum peel and main constituents. *Mater. Chem. Phys.* **2012**, *131*, 621–633. [[CrossRef](#)]
35. Zelinka, S.L.; Stone, D.S. The effect of tannins and pH on the corrosion of steel in wood extracts. *Mater. Corros.* **2011**, *62*, 739–744. [[CrossRef](#)]
36. Pugsley, V.A.; Korn, G.; Luyckx, S.; Sockel, H.G.; Heinrich, W.; Wolf, M.; Feld, H.; Schulte, R. The influence of a corrosive wood-cutting environment on the mechanical properties of hardmetal tools. *Int. J. Refract. Met. Hard Mater.* **2001**, *19*, 311–318. [[CrossRef](#)]
37. Winkelmann, H.; Badisch, E.; Llo, S.; Eglsaer, S. Corrosion behaviour of tool steels in tannic acids. *Mater. Corros.* **2009**, *60*, 192–198. [[CrossRef](#)]
38. Nigam, A.N.; Tripathi, R.P.; Dhoot, K. The effect of phosphoric acid on rust studied by mössbauer spectroscopy. *Corros. Sci.* **1990**, *30*, 799–803. [[CrossRef](#)]
39. Dehghani, A.; Ramezanzadeh, B.; Poshtiban, F.; Bahlakeh, G. Construction of a highly-effective/sustainable corrosion protective composite nanofilm based on Aminotris(methylphosphonic acid) and trivalent cerium ions on mild steel against chloride solution. *Constr. Build. Mater.* **2020**, *261*, 119838. [[CrossRef](#)]
40. Huang, X.; Wang, D.; Dong, Y. Corrosion resistance phosphate coating formed by steam assisted curing on cast Al-Si alloy. *Surf. Coat. Technol.* **2020**, *382*, 125242. [[CrossRef](#)]

41. Dehghani, A.; Poshtiban, F.; Bahlakeh, G.; Ramezanzadeh, B. Fabrication of metal-organic based complex film based on three-valent samarium ions-[bis (phosphonomethyl) amino] methylphosphonic acid (ATMP) for effective corrosion inhibition of mild steel in simulated seawater. *Constr. Build. Mater.* **2020**, *239*, 117812. [[CrossRef](#)]
42. Almeida, E.; Pereira, D.; Figueiredo, M.O.; Lobo, V.M.M.; Morcillo, M. The influence of the interfacial conditions on rust conversion by phosphoric acid. *Corros. Sci.* **1997**, *39*, 1561–1570. [[CrossRef](#)]
43. Feng, L.; Yuan, P. Corrosion protection mechanism of aluminum triphosphate modified by organic acids as a rust converter. *Prog. Org. Coat.* **2020**, *140*, 105508. [[CrossRef](#)]
44. Zhao, X.D.; Cheng, Y.F.; Fan, W.; Vladimir, C.; Volha, V.; Alla, T. Inhibitive performance of a rust converter on corrosion of mild steel. *J. Mater. Eng. Perform.* **2014**, *23*, 4102–4108. [[CrossRef](#)]
45. Gust, J. Application of infrared spectroscopy for investigation of rust phase component conversion by agents containing oak tannin and phosphoric acid. *Corrosion* **1991**, *47*, 453–457. [[CrossRef](#)]
46. Galvan, J.C., Jr.; Simancas, J.; Morcillo, M.; Bastidas, J.; Almeida, E.; Feliu, S. Effect of treatment with tannic, gallic and phosphoric acids on the electrochemical behaviour of rusted steel. *Electrochim. Acta* **1992**, *37*, 1983–1985. [[CrossRef](#)]
47. Fan, X.; Zhao, X. High-performance rust converter with a formula based on polyphosphoric acid and tannic acid. *Adv. Mater. Res.* **2011**, *150–151*, 1277–1281. [[CrossRef](#)]
48. Saji, V.S. Progress in rust converters. *Prog. Org. Coat.* **2019**, *127*, 88–99. [[CrossRef](#)]
49. Jamil, H.E.; Shrir, A.; Boulif, R.; Bastos, C.; Montemor, M.F.; Ferreira, M.G.S. Electrochemical behaviour of amino alcohol-based inhibitors used to control corrosion of reinforcing steel. *Electrochim. Acta* **2004**, *49*, 2753–2760. [[CrossRef](#)]
50. Wombacher, F.; Maeder, U.; Marazzani, B. Aminoalcohol based mixed corrosion inhibitors. *Cem. Concr. Comp.* **2004**, *26*, 209–216. [[CrossRef](#)]
51. Boughoues, Y.; Benamira, M.; Messaadia, L.; Ribouh, N. Adsorption and corrosion inhibition performance of some environmental friendly organic inhibitors for mild steel in HCl solution via experimental and theoretical study. *Colloids Surf. A* **2020**, *593*, 124610. [[CrossRef](#)]
52. Gupta, N.K.; Verma, C.; Quraishi, M.A.; Mukherjee, A.K. Schiff's bases derived from l-lysine and aromatic aldehydes as green corrosion inhibitors for mild steel: Experimental and theoretical studies. *J. Mol. Liq.* **2016**, *215*, 47–57. [[CrossRef](#)]
53. Yurt, A.; Ulutas, S.; Dal, H. Electrochemical and theoretical investigation on the corrosion of aluminium in acidic solution containing some schiff bases. *Appl. Surf. Sci.* **2006**, *253*, 919–925. [[CrossRef](#)]
54. Christov, M.; Popova, A. Adsorption characteristics of corrosion inhibitors from corrosion rate measurements. *Corros. Sci.* **2004**, *46*, 1613–1620. [[CrossRef](#)]
55. Jeyaprabha, C.; Sathiyarayanan, S.; Venkatachari, G. Corrosion inhibition of pure iron in 0.5 M H₂SO₄ solutions by ethanolamines. *Appl. Surf. Sci.* **2005**, *246*, 108–116. [[CrossRef](#)]
56. Verma, C.; Ebenso, E.E.; Quraishi, M.A. Molecular structural aspects of organic corrosion inhibitors: Influence of –CN and –NO₂ substituents on designing of potential corrosion inhibitors for aqueous media. *J. Mol. Liq.* **2020**, *316*, 113874. [[CrossRef](#)]
57. Al-Mehthel, M.; Al-Dulaijan, S.; Al-Idi, S.H.; Shameem, M.; Ali, M.R.; Maslehuddin, M. Performance of generic and proprietary corrosion inhibitors in chloride-contaminated silica fume cement concrete. *Constr. Build. Mater.* **2009**, *23*, 1768–1774. [[CrossRef](#)]
58. Chipanina, N.N.; Aksamentova, T.N.; Adamovich, S.N.; Albanov, A.I.; Mirskova, A.N.; Mirskov, R.G.; Voronkov, M.G. The proton transfer and hydrogen bonding complexes of (2-hydroxyethyl)amines with acids: A theoretical study. *Comput. Theor. Chem.* **2012**, *985*, 36–45. [[CrossRef](#)]
59. Mohammad, S.S.; Jamileh, S.Y.; Hoda, H. Fe₂O₃/Fe₃O₄/PANI/MWCNT nanocomposite with the optimum amount and uniform orientation of Fe₂O₃/Fe₃O₄ NPs in polyaniline for high microwave absorbing performance. *J. Alloys Compd.* **2020**, *843*, 156052. [[CrossRef](#)]
60. Poormirzaei, N. Synthesis and characterization of a novel Pyrrole-2-carboxylic acid functionalized magnetic Fe₃O₄ as a nanocatalyst for synthesis and antibacterial activities of novel isoxazolo[4,3-e]indazole derivatives. *J. Mol. Struct.* **2021**, *1227*, 129265. [[CrossRef](#)]
61. Guo, H.; Li, Z.; Lin, S.; Li, D.; Jiang, N.; Wang, H.; Han, J.; Li, J. Multi-catalysis induced by pulsed discharge plasma coupled with graphene-Fe₃O₄ nanocomposites for efficient removal of ofloxacin in water: Mechanism, degradation pathway and potential toxicity. *Chemosphere* **2021**, *265*, 129089. [[CrossRef](#)] [[PubMed](#)]
62. Li, Q.; Li, R.; Ma, X.; Sarkar, B.; Sun, X.; Bolan, N. Comparative removal of As(V) and Sb(V) from aqueous solution by sulfide-modified α -FeOOH. *Environ. Pollut.* **2020**, *267*, 115658. [[CrossRef](#)] [[PubMed](#)]
63. Rahimi, S.; Moattari, R.M.; Rajabi, L.; Derakhshan, A.A.; Keyhani, M. Iron oxide/hydroxide (α , γ -FeOOH) nanoparticles as high potential adsorbents for lead removal from polluted aquatic media. *J. Ind. Eng. Chem.* **2015**, *23*, 33–43. [[CrossRef](#)]
64. Ristic, M.; Music, S.; Godec, M. Properties of γ -FeOOH, α -FeOOH and α -Fe₂O₃ particles precipitated by hydrolysis of Fe³⁺ ions in perchlorate containing aqueous solutions. *J. Alloys Compd.* **2006**, *417*, 292–299. [[CrossRef](#)]